

Aspects of the computational testing of the mechanical properties of microheterogeneous material samples[§]

T. I. Zohdi^{*,†} and P. Wriggers[‡]

Institut für Baumechanik und Numerische Mechanik, Appelstrasse 9A, 30167 Hannover, Germany

SUMMARY

In this paper we investigate topics related to the numerical simulation of the testing of mechanical responses of samples of microheterogeneous solid material. Consistent with what is produced in dispersion manufacturing methods, the microstructures considered are generated by randomly distributing aggregates of particulate material throughout an otherwise homogeneous matrix material. Therefore, the resulting microstructures are irregular and non-periodic. A primary problem in testing such materials is the fact that only finite-sized samples can be tested, leading to no single response, but a distribution of responses. In this work, a technique employing potential energy principles is presented to interpret the results of testing groups of samples. Three-dimensional numerical examples employing the finite element method are given to illustrate the overall analysis and computational testing process. Copyright © 2001 John Wiley & Sons, Ltd.

KEY WORDS: material testing; random heterogeneous materials

1. INTRODUCTION

Many structural materials exhibit microheterogeneities which can have significant influence on the macroscopic properties. The macroscopic characteristics are the aggregate response of a collection of various constituents, for example, particulate matter suspended in a binding matrix material. In many applications tailored material properties are desired. The general approach in the design of such materials is to enhance or modify a matrix material's properties by the addition of fine particles of different material to produce a desired aggregate effect. A large percentage of such materials are manufactured using dispersion processes, by which the reinforcing material is incorporated in loose form into the matrix material (Figure 1). We shall be primarily concerned with these types of heterogeneous materials in this work. Because such systems exhibit poor wetting, mechanical force is required to combine the phases, generally through stirring. One of the simplest dispersion processes in current use is the Vortex method,

*Correspondence to: T. I. Zohdi, Institut für Baumechanik und Numerische Mechanik, Appelstrasse 9A, 30167 Hannover, Germany

[†]E-mail: zohdi@ibnm.uni-hannover.de

[‡]E-mail: wriggers@ibnm.uni-hannover.de

[§]Dedicated to Professor Dietmar Gross on the occasion of his 60th birthday.

Received 19 November 1999

Revised 4 July 2000

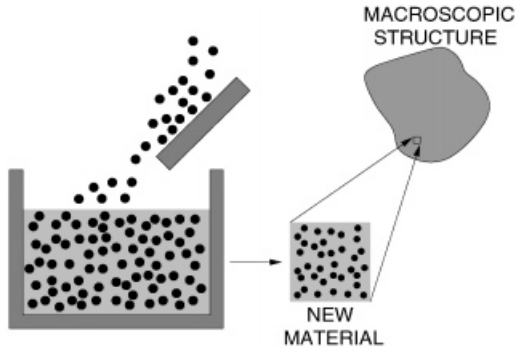


Figure 1. Modifying a material with particulate additives.

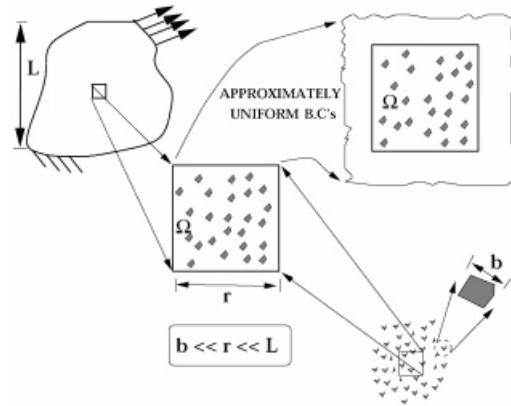


Figure 2. Size requirements of a representative volume element.

which consists of vigorous stirring of the liquid matrix material and the addition of particles in a vortex. The resulting particulate positions and orientation (relevant when not spherical) are random. This method is currently one of the most inexpensive processes in which to produce particulate-modified materials. Such materials can be produced in large quantities, which can then be further processed, for example via casting or extrusion. We refer the reader to a review found in Reference [1] for more details.

If one were to attempt to directly numerically simulate the response of an entire macroscopic engineering structure, incorporating all of the heterogeneities, a problem of extreme computational complexity would arise. Even if it were possible to solve the system of equations derived from a spatial discretization of such a structure, the problem of ‘knowing what is inside’ is virtually impossible to ascertain non-destructively. Regardless of whether those obstacles were removed, the data to post-process from such computations would be of such complexity that it is unlikely that any useful information could be extracted. Historically, these types of problems have been dealt with by regularization methods generally referred to as ‘homogenization’. In engineering the main interest has been in a certain type of homogenization, that of volumetric averaging type, usually referred to as the theory of effective properties. We do not attempt to survey this well-explored subject. Reviews of this classical research area can be found in the somewhat standard reference works of Mura [2], Nemat-Nasser and Hori [3] or Jikov *et al.* [4]. The classical goal in the analysis of heterogeneous solid materials is to determine an effective macroscopic linear elasticity tensor, \mathbb{E}^* , a relation between averages, $\langle \boldsymbol{\sigma} \rangle_{\Omega} = \mathbb{E}^* : \langle \boldsymbol{\varepsilon} \rangle_{\Omega}$, where $\langle \cdot \rangle_{\Omega} \stackrel{\text{def}}{=} (1/|\Omega|) \int_{\Omega} \cdot d\Omega$, and where $\boldsymbol{\sigma}$ and $\boldsymbol{\varepsilon}$ are the stress and strain tensor fields within a statistically representative volume element (RVE) with volume $|\Omega|$. The usual philosophy is to consider the RVE as small enough to be considered as a material point with respect to the size of the macrodomain under analysis, but large enough to be a statistically representative sample of the microstructure (Figure 2). Classical analyses usually consider the RVE to be infinitely large in comparison to the intrinsic length scales of the microstructure. However, on a practical level, when computing effective mechanical responses of materials possessing random heterogeneous microstructure, one can only test finite-sized

samples. Therefore, responses computed from equal sized samples exhibit deviations from one another. This issue is one of the primary concerns in this work.

The relatively recent increase in computer power has brought with it the reality that numerical simulations can play a significant and complementary role to analytical and laboratory techniques used in testing heterogeneous materials. In this paper we are concerned with the development of computational testing processes for multiple samples possessing irregular microstructure. By direct computation, for example using the finite element method, one can eliminate the need for most approximate methods of homogenization, and simultaneously obtain information on local microstress fields, if desired. The results of such tests require certain methods of interpretation, which are introduced later in the work. The outline of this paper is as follows. In Section 2 background information is given pertaining to effective properties. In Section 3 numerical discretization is discussed. In Section 4 we offer some examples illustrating the process and its application to testing a material with random material microstructure. In Section 5 a method of interpretation for the results, based upon classical energy minimization principles, is presented. Finally, in Section 6 concluding remarks are given.

2. TESTING MICROHETEROGENEOUS MATERIAL SAMPLES

We consider a structure which occupies an open bounded domain in $\Omega \in \mathbb{R}^3$. Its boundary is denoted $\partial\Omega$. The body is in static equilibrium under the action of body forces, \mathbf{f} , and surface tractions, \mathbf{t} . The boundary $\partial\Omega = \bar{\Gamma}_u \cup \bar{\Gamma}_t$ consists of a part Γ_u and a part Γ_t on which displacements and tractions are, respectively, prescribed. The mechanical properties of the heterogeneous material are characterized by a spatially varying elasticity tensor $\mathbb{E} \in \mathbb{R}^{3^2 \times 3^2}$ which is assumed to satisfy $a_+ \boldsymbol{\varepsilon} : \boldsymbol{\varepsilon} \geq \boldsymbol{\varepsilon} : \mathbb{E}(\mathbf{x}) : \boldsymbol{\varepsilon} \geq a_- \boldsymbol{\varepsilon} : \boldsymbol{\varepsilon}$, $\forall \boldsymbol{\varepsilon} \in \mathbb{R}^{3 \times 3}$, $\boldsymbol{\varepsilon} = \boldsymbol{\varepsilon}^T$, $\infty > a_-$, $a_+ > 0$, $\forall \mathbf{x} \in \Omega$, where $E_{ijkl}(\mathbf{x}) = E_{jikl}(\mathbf{x}) = E_{ijlk}(\mathbf{x}) = E_{klij}(\mathbf{x})$, $1 \leq i, j, k, l \leq 3$, $E_{ijkl}(\mathbf{x})$ being the Cartesian components of \mathbb{E} at point \mathbf{x} . Following standard notation, we denote $H^1(\Omega)$ as the usual space of functions with generalized partial derivatives of order ≤ 1 in $L^2(\Omega)$. We define $\mathbf{H}^1(\Omega) \stackrel{\text{def}}{=} [H^1(\Omega)]^3$ as the space of vector-valued functions whose components are in $H^1(\Omega)$, and we denote $\mathbf{L}^2(\Omega) \stackrel{\text{def}}{=} [L^2(\Omega)]^3$. We shall use the symbol ' $\mathbf{u}|_{\partial\Omega}$ ' for boundary values. The data are assumed to be such that $\mathbf{f} \in \mathbf{L}^2(\Omega)$ and $\mathbf{t} \in \mathbf{L}^2(\Gamma_t)$, but less smooth data can be considered without complications.

We consider a sample of material (Figure 3), with domain Ω , under a given set of specified boundary loadings. The variational boundary value problem is

<p>Find $\mathbf{u} \in \mathbf{H}^1(\Omega)$, $\mathbf{u} _{\Gamma_u} = \mathbf{d}$, such that</p> $\int_{\Omega} \nabla \mathbf{v} : \mathbb{E} : \nabla \mathbf{u} \, d\Omega = \int_{\Omega} \mathbf{f} \cdot \mathbf{v} \, d\Omega + \int_{\Gamma_t} \mathbf{t} \cdot \mathbf{v} \, dA \quad \forall \mathbf{v} \in \mathbf{H}^1(\Omega), \mathbf{v} _{\Gamma_u} = 0$	(1)
--	-----

For convenience, the domain Ω in Figure 3 is shown as cubical, although this is not necessary.

A compact micro/macroenergy equivalence statement, $\langle \boldsymbol{\sigma} : \boldsymbol{\varepsilon} \rangle_{\Omega} = \langle \boldsymbol{\sigma} \rangle_{\Omega} : \langle \boldsymbol{\varepsilon} \rangle_{\Omega}$, known as Hill's condition [5], dictates the size requirements placed on the RVE. This macro/micro-energy condition must be realizable by the fields within the RVE for the sample to admit to an

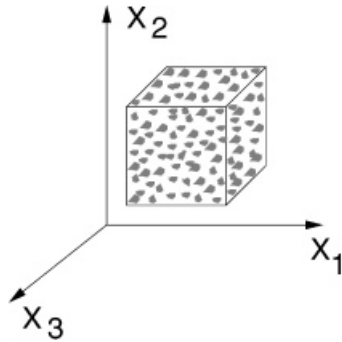


Figure 3. A cubical sample of microheterogeneous material.

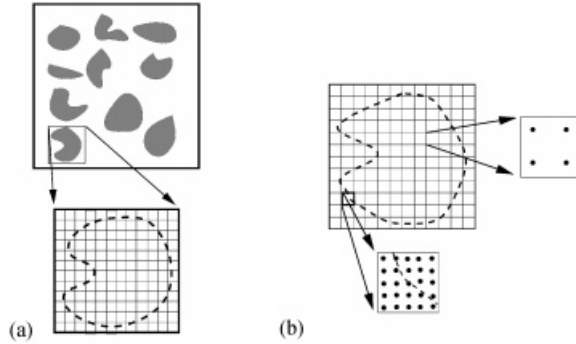


Figure 4. (a) Unaligned meshing; (b) material discontinuities within an element.

energetically sensible homogenization. For any perfectly bonded heterogeneous body, in the absence of body forces, two physically important loading states satisfy Hill’s condition. They are $(\mathbf{f} = \mathbf{0})$ (1) pure linear displacements of the form $\mathbf{u}|_{\partial\Omega} = \boldsymbol{\varepsilon} \cdot \mathbf{x} \Rightarrow \langle \boldsymbol{\varepsilon} \rangle_{\Omega} = \boldsymbol{\varepsilon}$ and (2) pure tractions in the form $\mathbf{t}|_{\partial\Omega} = \boldsymbol{\mathcal{L}} \cdot \mathbf{n} \Rightarrow \langle \boldsymbol{\sigma} \rangle_{\Omega} = \boldsymbol{\mathcal{L}}$; where $\boldsymbol{\varepsilon}$ and $\boldsymbol{\mathcal{L}}$ are constant strain and stress tensors, respectively. Clearly, for Hill’s conditions to be satisfied within a macroscopic body under non-uniform external loading, the sample must be large enough to have small boundary field fluctuations relative to its size. Therefore, applying (1)- or (2)-type boundary conditions to a large sample is a convenient way of reproducing approximately what may be occurring in a statistically representative microscopic sample of material in a macroscopic body. Explicitly, to determine \mathbb{E}^* , one specifies six linearly independent loading of the form, (1) $\mathbf{u}|_{\partial\Omega} = \boldsymbol{\varepsilon}^{(1 \rightarrow VI)} \cdot \mathbf{x}$ or (2) $\mathbf{t}|_{\partial\Omega} = \boldsymbol{\mathcal{L}}^{(1 \rightarrow VI)} \cdot \mathbf{n}$ where $\boldsymbol{\varepsilon}^{(1 \rightarrow VI)}$ and $\boldsymbol{\mathcal{L}}^{(1 \rightarrow VI)}$ are symmetric second-order strain and stress tensors, with spatially constant components. Each independent loading state provides six equations, for a total of 36, which are used to determine the tensor relation between average stress and strain, \mathbb{E}^* . If the effective response is assumed isotropic then only one test loading (instead of six), containing non-zero dilatational ($\text{tr } \boldsymbol{\sigma}/3$ and $\text{tr } \boldsymbol{\varepsilon}/3$) and deviatoric components ($\boldsymbol{\sigma}' \stackrel{\text{def}}{=} \boldsymbol{\sigma} - (\text{tr } \boldsymbol{\sigma}/3)\mathbf{I}$ and $\boldsymbol{\varepsilon}' \stackrel{\text{def}}{=} \boldsymbol{\varepsilon} - (\text{tr } \boldsymbol{\varepsilon}/3)\mathbf{I}$), is necessary to determine the effective bulk and shear moduli:

$$3\kappa^* \stackrel{\text{def}}{=} \frac{\langle \text{tr } \boldsymbol{\sigma}/3 \rangle_{\Omega}}{\langle \text{tr } \boldsymbol{\varepsilon}/3 \rangle_{\Omega}} \quad \text{and} \quad 2\mu^* \stackrel{\text{def}}{=} \sqrt{\frac{\langle \boldsymbol{\sigma}' \rangle_{\Omega} : \langle \boldsymbol{\sigma}' \rangle_{\Omega}}{\langle \boldsymbol{\varepsilon}' \rangle_{\Omega} : \langle \boldsymbol{\varepsilon}' \rangle_{\Omega}}} \tag{2}$$

We note that even if the aggregate response is not purely isotropic, one can always interpret the above expressions as generalizations of isotropic responses.

3. NUMERICAL DISCRETIZATION

In order to computationally simulate the effective responses, our choice for spatial discretization is the finite element method. There are essentially two choices to mesh the microstructure with the finite element method, an unaligned or an aligned approach. We refer to an unaligned

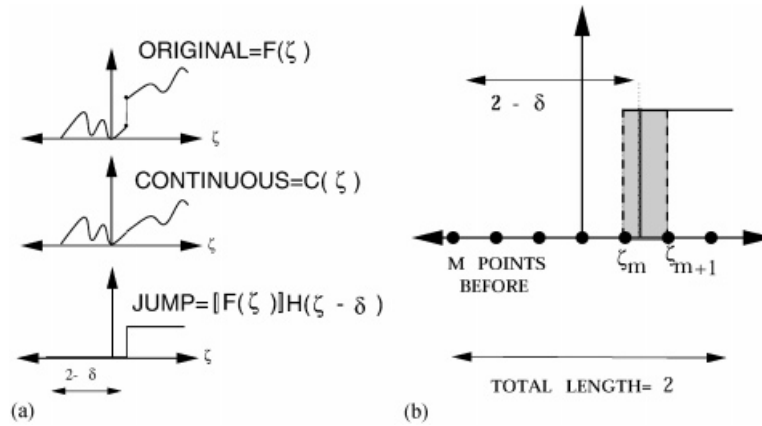


Figure 5. (a) Decomposition of the discontinuous integrand on the reference element level; (b) Gaussian quadrature points.

approach as one which does not require the finite element boundaries to coincide with material interfaces when meshing the internal geometry (Figure 4). This leads to material discontinuities within the finite elements. An aligned approach would impose that the element boundaries coincide with material interfaces and therefore the elements have no material discontinuities within them. There are advantages and disadvantages of both approaches. Unaligned meshing has the advantages of rapid generation of structured internal meshes and consequently no finite element distortion arising from the microstructure. This is critical to computational performance if iterative solvers are to be used. Further discussion on such solvers, which are used in this work, is given in Appendix C. The aligned meshing usually will require less finite elements than the unaligned approach for the same pointwise accuracy. However, the disadvantages are the mesh generation for irregular microstructures in three dimensions. Even if such microstructures can be meshed in an aligned manner, the finite element distortion leads to stiffness matrix ill-conditioning and possible element instability (shape non-convexity). For previous numerical studies and comparisons between the approaches, see Reference [6]. Here our emphasis is on admitting general irregular microstructures, and rapidly evaluating them during the testing process, thus we have taken the unaligned approach, which we discuss in more detail next.

3.1. Topological error

Inherent in the unaligned approach is the integration of discontinuous integrands (Figure 5). The topology is not embedded into the finite element a priori, as it would be in an aligned approach, via isoparametric maps onto material interfaces. To some extent if the elements are much smaller than the particle length scales, the topology will be approximately resolved. However, one can improve this representation (Figure 4). Since the finite element method is an integral-based method, the quadrature rules can be increased in an element by element fashion to better capture the geometry in elements with material discontinuities. A primary question is: If there is an integrand discontinuity in a finite element, how high should the quadrature rules be to perform accurate integration?

3.1.1. *Topological error bounds for unaligned meshing.* We first consider a one dimensional reference element as shown in Figure 5. We assume that the elements are small compared to the length scales of the particulate matter (this is automatically dictated by a subspecial approximation error estimator presented in the next section) and as a consequence we assume that there is at most one discontinuity within the element. However, this assumption makes no difference in practice. We consider integrands, $F(\zeta)$, defined on the reference element, with jump discontinuity at δ , which admit the following decomposition:

$$F(\zeta) = \underbrace{C(\zeta)}_{\text{continuous}} + \llbracket F(\delta) \rrbracket \underbrace{H(\zeta - \delta)}_{\text{jump}} \tag{3}$$

where ζ is the local coordinate, and $\llbracket (\cdot) \rrbracket \stackrel{\text{def}}{=} (\cdot)_+ - (\cdot)_-$ is the jump operator. Integrating over the reference element, we have

$$\int_{-1}^1 F(\zeta) d\zeta = \int_{-1}^1 (C(\zeta) + \llbracket F(\delta) \rrbracket H(\zeta - \delta)) d\zeta \tag{4}$$

We perform a straightforward Gauss–Legendre quadrature, with G quadrature points, where m points lie before the discontinuity at δ (Figure 5). We assume that the continuous function, possibly a polynomial, can be integrated exactly, or nearly exactly, with standard quadrature

$$\int_{-1}^1 C(\zeta) d\zeta \approx \sum_{i=1}^G C(\zeta_i) w_i \tag{5}$$

where w_i are the Gauss weights and where ζ_i are the Gauss point locations. The remainder is the discontinuous part

$$\llbracket F(\delta) \rrbracket \int_{-1}^1 H(\zeta - \delta) d\zeta = \llbracket F(\delta) \rrbracket (1 - \delta) \tag{6}$$

We may write

$$\llbracket F(\delta) \rrbracket \sum_{i=1}^G H(\zeta_i - \delta) w_i = \llbracket F(\delta) \rrbracket \sum_{i=1}^m 0 \times w_i + \llbracket F(\delta) \rrbracket \sum_{i=m+1}^G 1 \times w_i \tag{7}$$

As a consequence, the integration error is

$$\begin{aligned} & \left| \int_{-1}^{-1} F(\zeta) d\zeta - \left(\sum_{i=1}^G (C(\zeta_i) + \llbracket F(\delta) \rrbracket H(\zeta_i - \delta)) w_i \right) \right| \\ &= \llbracket F(\delta) \rrbracket \left| (2 - \delta) - \left(2 - \sum_{i=m+1}^G w_i \right) \right| \\ &= \llbracket F(\delta) \rrbracket \left| \left(\sum_{i=m+1}^G w_i - \delta \right) \right| \\ &\leq \llbracket F(\delta) \rrbracket \left| \left(\sum_{i=m+1}^G w_i - \sum_{i=m}^G w_i \right) \right| \\ &\leq \llbracket F(\delta) \rrbracket \max_i w_i \max_j |\zeta_j - \zeta_{j\pm 1}| \end{aligned} \tag{8}$$

Table I. Integration error bound behaviour for a unit jump. Domain: $(-1, 1) \times (-1, 1) \times (-1, 1)$, for a 3-D step function discontinuity ($8 = 2 \times 2 \times 2 =$ volume of the reference element).

Gauss rule	Bound = $\frac{(5.07G^{-1.82})^3}{8}$
$2 \times 2 \times 2$	0.37
$3 \times 3 \times 3$	0.04
$4 \times 4 \times 4$	0.008
$5 \times 5 \times 5$	0.002

In order to bound the dependence of the largest quadrature weight, w_i , and the maximum possible distance $|\zeta_i - \zeta_{i\pm 1}|$ in the interval $(-1, 1)$, with the Gauss–Legendre rule, we least squares curve-fit (Gauss rules of $1 \leq G \leq 10$) with the following results:

$$\max_{i \leq g} w_i \approx 1.93G^{-0.795}, \quad \max_{\zeta_m \in (-1, 1)} |\zeta_i - \zeta_{i\pm 1}| \approx 2.6G^{-1.02}, \quad R^2 = 0.99 \tag{9}$$

where $R^2 = 1.0$ indicates a perfect regression value of the curve fit. The product is

$$\max_i w_i \max_i |\zeta_i - \zeta_{i\pm 1}| \approx 5.07G^{-1.82} \tag{10}$$

Simple three-dimensional estimates can be made by applying this procedure in all three directions on a reference element. It is clear that the error is directly related to the distance between Gauss point sampling locations. Table I illustrates the bound on this error in Equation (9). *The ‘oversampling’ only takes place in elements where there is a discontinuity* (Figure 4(b)). In elements with no material discontinuities the canonical rules should be used. This reduces computation time in forming the stiffness matrix. Consequently, we apply a ‘2/5’ rule, i.e. a $2 \times 2 \times 2$ Gauss rule if there is no discontinuity in the element, and a $5 \times 5 \times 5$ rule if there is a discontinuity. We emphasize that this procedure is used simply to integrate quantities with discontinuities accurately. Earlier related numerical investigations of this process can be found in Reference [6].

3.2. A Galerkin error monitor

In order to judge the quality of the numerical results, we need an indication of the Galerkin ‘subspatial’ approximation error. Under standard assumptions the classical a priori error estimate for the finite element method is

$$\begin{aligned} \|\mathbf{u} - \mathbf{u}^h\|_{E(\Omega)} &\leq \mathcal{C}(\mathbf{u}, p) h^{\min(s-1, p)} \stackrel{\text{def}}{=} r \\ \|\mathbf{u} - \mathbf{u}^h\|_{E(\Omega)}^2 &\stackrel{\text{def}}{=} \int_{\Omega} \nabla(\mathbf{u} - \mathbf{u}^h) : \mathbb{E} : \nabla(\mathbf{u} - \mathbf{u}^h) \, d\Omega \end{aligned} \tag{11}$$

Here p is the (complete) polynomial order of the finite element method used, s is the regularity of the exact solution and \mathcal{C} is a global constant dependent on the exact solution and the polynomial approximation, but independent of h , the maximum element diameter.

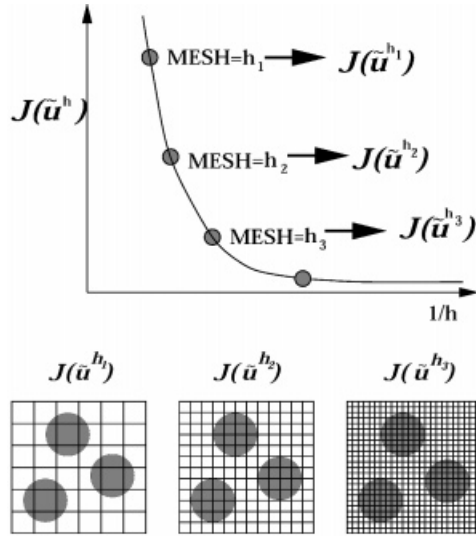


Figure 6. Successively refined (embedded) meshes used to estimate the error.

Related forms of this estimate hold locally, but with constants that are element dependent. The smoothness of the solution is no better than $s = 1.5$ ($r = 0.5$) for elements containing material discontinuities. However, the solution can be quite smooth, i.e. $s > 1.5$ ($r > 0.5$), for elements with no material discontinuities. For simplicity, we employ the h -version finite element method, i.e. successive mesh subdivision using trilinear hexahedra ($p = 1$), and therefore $r = 1$ in elements with no discontinuities. More remarks are given in Appendix A. We recall a well-known property,

$$\| \mathbf{u} - \mathbf{u}^h \|_{E(\Omega)}^2 = 2(\mathcal{J}(\mathbf{u}^h) - \mathcal{J}(\mathbf{u})) \tag{12}$$

$$\mathcal{J}(\mathbf{u}) \stackrel{\text{def}}{=} \frac{1}{2} \int_{\Omega} \nabla \mathbf{u} : \mathbb{E} : \nabla \mathbf{u} \, d\Omega - \int_{\Omega} \mathbf{f} \cdot \mathbf{u} \, d\Omega - \int_{\Gamma_t} \mathbf{t} \cdot \mathbf{u} \, dA$$

which is merely a restatement of the principle of minimum potential energy. By solving the boundary value problem associated for a given sample for three successively finer meshes, $h_1 > h_2 > h_3$, with the following property (see Figure 6):

$$\mathcal{J}(\mathbf{u}^{h_1}) \geq \mathcal{J}(\mathbf{u}^{h_2}) \geq \mathcal{J}(\mathbf{u}^{h_3}) \geq \mathcal{J}(\mathbf{u}^{h=0}) \tag{13}$$

we can set up the following system of equations for unknown constants a, b , and c :

$$\begin{aligned} ah_1^\alpha + bh_1^\beta + c &= \mathcal{J}(\mathbf{u}^{h_1}) \\ ah_2^\alpha + bh_2^\beta + c &= \mathcal{J}(\mathbf{u}^{h_2}) \\ ah_3^\alpha + bh_3^\beta + c &= \mathcal{J}(\mathbf{u}^{h_3}) \end{aligned} \tag{14}$$

where the exponents α and β are selected to reflect the estimated regularity of the solution in the elements. In the case of using trilinear hexahedra we are led for the logical choice of exponents: $\alpha = 2r = 2$, representing elements with no material discontinuities, and $\beta = 2r = 1$, representing elements with material discontinuities. It is clear that $c \approx \mathcal{J}(\mathbf{u}^{h=0})$, and we can thus define the following quantity to monitor the Galerkin error:

$$\zeta \stackrel{\text{def}}{=} \frac{2(\mathcal{J}(\mathbf{u}^{h_3}) - c)}{\mathcal{E} : \langle \mathbb{E} \rangle_{\Omega} : \mathcal{E} |\Omega|} \tag{15}$$

In summary, to monitor the discretization error, we apply the following algorithm:

<p><i>Step 1:</i> Coarse mesh $h_1 : \mathbf{u}^{h_1} \Rightarrow \ \mathbf{u}^{h_1}\ _{E(\Omega)}^2$</p> <p><i>Step 2:</i> Finer mesh $h_2 = K_1 \times h_1 : \mathbf{u}^{h_2} \Rightarrow \ \mathbf{u}^{h_2}\ _{E(\Omega)}^2 \quad (0 < K_1 < 1)$</p> <p><i>Step 3:</i> Finer mesh $h_3 = K_2 \times h_2 : \mathbf{u}^{h_3} \Rightarrow \ \mathbf{u}^{h_3}\ _{E(\Omega)}^2 \quad (0 < K_2 < 1)$</p> <p><i>Step 4:</i> Compute a, b and $c \Rightarrow \zeta \stackrel{\text{def}}{=} \frac{2(\mathcal{J}(\mathbf{u}^{h_3}) - c)}{\mathcal{E} : \langle \mathbb{E} \rangle_{\Omega} : \mathcal{E} \Omega }$</p>	<p style="text-align: right;">(16)</p>
--	--

These operations are performed for each sample, since they each have different random microstructure.

4. OVERALL TESTING PROCESS: NUMERICAL EXAMPLES

A typical example of a composite material combination is that of an aluminium matrix (77.9, 24.9 GPa) embedded with (stiffening) Boron particles (230, 172 GPa). This is a widely used composite due to its light weight. We chose AL/Bo as a material combination which exhibits significant enough mismatch in the mechanical properties to be representative of a wide range of cases. All tests were run on a single IBM RISC 6000 workstation. Comparable hardware is available in most academic and industrial work places, therefore such simulations are easily reproducible elsewhere for other parameter selections.

4.1. Successive sample enlargement

In a first set of tests, the number of particles contained in a sample were increased holding the volume fraction constant. During the tests, we repeatedly refined the mesh to obtain invariant macroscopic responses. A sample/particle size ratio was used as a microstructural control parameter. This was done by defining a subvolume size

$$V \stackrel{\text{def}}{=} \frac{L \times L \times L}{N} \tag{17}$$

where N is the number of particles in the entire sample and where L is the length of the (cubical $L \times L \times L$) sample. A generalized diameter was defined, d , which was the diameter of the smallest sphere that can enclose a single particle, of possibly non-spherical shape, if desired.

Table II. Results of successive sample ‘enlargements’. Five tests, each with a different random distribution, were performed at each sample/particulate size ratio level to obtain somewhat representative data.

Part	d/L	Dof	W (Gpa)	κ^* (GPa)	μ^* (GPa)
2	0.595	5184	0.001444	98.2	46.7
4	0.472	10 125	0.001408	97.3	44.3
8	0.375	20 577	0.001386	96.5	43.2
16	0.298	41 720	0.001375	96.2	42.5
32	0.236	81 000	0.001365	95.9	41.6
64	0.188	151 959	0.001358	95.7	41.4

The ratio between the generalized diameter and the subvolume was defined by

$$\zeta \stackrel{\text{def}}{=} \frac{d}{V^{1/3}} \quad (18)$$

For a variety of numerical tests, discussed momentarily, the typical mesh density to deliver invariant volumetrically averaged responses was $9 \times 9 \times 9$ trilinear finite element hexahedra (approximately 2200–3000 degrees of freedom) *per particle*. We used $\zeta = 0.75$, which resulted in a (fixed) volume fraction of approximately 22 per cent. The following particle per sample sequence was used to study the dependence of the effective responses on the sample size: 2 (5184 DOF), 4 (10 125 DOF), 8 (20 577 DOF), 16 (41 720 DOF), 32 (81 000 DOF) and 64 (151 959 DOF) particles. In order to get more reliable response data for each particle number set, the tests were performed five times (each time with a different particulate distribution) and the responses averaged. Throughout the tests, we considered a single combined boundary loading satisfying Hill’s condition, $\mathcal{E}_{ij} = 0.001$, $i, j = 1, 2, 3$:

$$\begin{bmatrix} u_1 |_{\partial\Omega} \\ u_2 |_{\partial\Omega} \\ u_3 |_{\partial\Omega} \end{bmatrix} = \underbrace{\begin{bmatrix} \mathcal{E}_{11} & \mathcal{E}_{12} & \mathcal{E}_{13} \\ \mathcal{E}_{12} & \mathcal{E}_{22} & \mathcal{E}_{23} \\ \mathcal{E}_{31} & \mathcal{E}_{32} & \mathcal{E}_{33} \end{bmatrix}}_{\mathcal{E}} \begin{bmatrix} x_1 \\ x_2 \\ x_3 \end{bmatrix} \quad (19)$$

We tracked the strain energy, as well as κ^* and μ^* , as defined in Equation (2). Table II depicts the dependency of the responses with growth in particle number. Justified by the somewhat ad hoc fact that for three successive enlargements of the number of particles, i.e. 16, 32 and 64 particle samples, the responses differed from one another, on average, by less than 1 per cent, we selected the 20-particle microstructures for further tests. We remark that we applied a ‘2/5’ rule, i.e. a $2 \times 2 \times 2$ Gauss rule if there is no discontinuity in the element, and a $5 \times 5 \times 5$ rule if there is a discontinuity, which is consistent with the earlier derivation in the work (Table I). The microstructure, as seen by this mesh density, is shown in Figure 7.

4.2. Multiple sample tests

For further tests, we simulated 100 different samples, each time with a different random distribution of 20 non-intersecting particles occupying 22 per cent ($\zeta = 0.75$). Consistent with

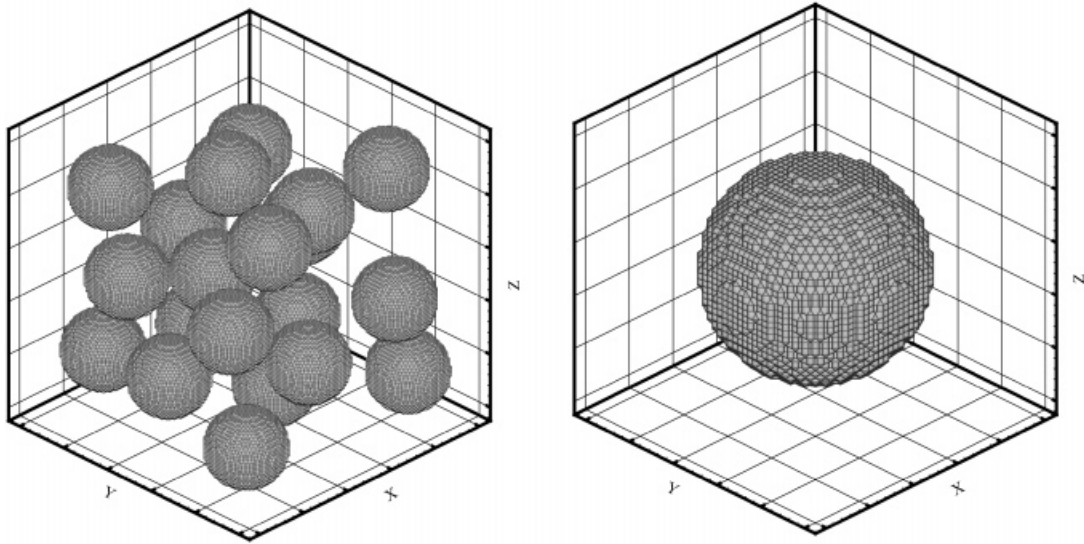


Figure 7. Top: a random microstructure consisting of 20 non-intersecting Boron spheres, occupying approximately 22 per cent of the volume in an aluminium matrix, as seen by the algorithm with a $24 \times 24 \times 24$ trilinear hexahedra mesh density for a total of 46 875 degrees of freedom (approximately $9 \times 9 \times 9$ hexahedra or 2344 degrees of freedom per element). A ‘2/5’ rule, i.e. a $2 \times 2 \times 2$ Gauss rule if there is no discontinuity in the element, and a $5 \times 5 \times 5$ rule if there is a discontinuity, was used. Bottom: a zoom on one particle.

the previous test’s mesh densities per particle, we used a $24 \times 24 \times 24$ mesh ($9 \times 9 \times 9$ trilinear hexahedra or 2344 dof per particle, 46 875 dof per test sample). The numerical error monitor, ξ , which measures microscopic differences (described in Box 16), was constructed for the each sample with a $24 \times 24 \times 24$ mesh density by using a mesh sequence of embedded finite element meshes: $6 \times 6 \times 6$, $12 \times 12 \times 12$ and $24 \times 24 \times 24$ (Figure 6). The $24 \times 24 \times 24$ mesh was used in all final computations for each sample, with an accompanying ξ computed each time. The plots of the behaviour of the various quantities of interest are shown in Figures 8–17. The averages, standard deviations and maximum/minimum of these quantities are tabulated in Table III. For the 100 sample tests, with 20 particles per sample, the results for the effective responses were

$$\begin{aligned}
 91.37 &= \langle \kappa^{-1} \rangle_{\Omega}^{-1} \leq \tilde{\kappa}^* = 96.17 \leq \langle \kappa \rangle_{\Omega} = 111.79 \\
 30.76 &= \langle \mu^{-1} \rangle_{\Omega}^{-1} \leq \tilde{\mu}^* = 42.35 \leq \langle \mu \rangle_{\Omega} = 57.68
 \end{aligned}
 \tag{20}$$

where $\tilde{\kappa}^*$ and $\tilde{\mu}^*$ are the averaged effective responses from the 100 tests, and where the lower and upper bounds are, respectively, the classical Reuss [7] and Voigt [8] bounds. We also

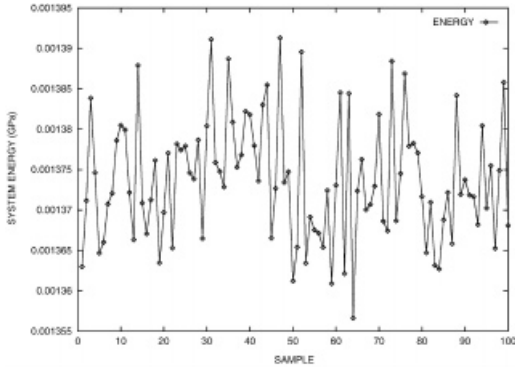


Figure 8. One-hundred samples: the energy responses, $W = (1/|\Omega|) \int_{\Omega} \nabla \mathbf{u} : \mathbb{E} : \nabla \mathbf{u} d\Omega$ (GPa), of a block with 20 randomly distributed Boron spheres embedded in an aluminium matrix. Each point represents the results of one test.

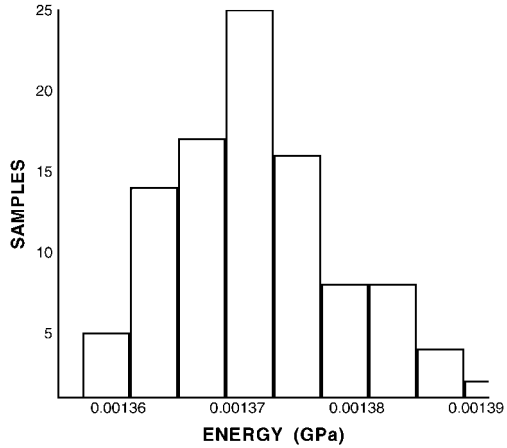


Figure 9. One-hundred samples: the corresponding histogram for the variations in energy, $W = (1/|\Omega|) \int_{\Omega} \nabla \mathbf{u} : \mathbb{E} : \nabla \mathbf{u} d\Omega$ (GPa).

compared the computed results to the well-known Hashin–Shtrikman bounds [9, 10] which are, strictly speaking, *only applicable* to asymptotic cases of an infinite (sample length)/(particulate length) ratio and purely isotropic macroscopic responses. The ‘bounds’ were as follows:

$$\begin{aligned}
 94.32 = \underbrace{\kappa_1 + \frac{v_2}{\frac{1}{\kappa_2 - \kappa_1} + \frac{3(1-v_2)}{3\kappa_1 + 4\mu_1}}}_{\text{bulk modulus H/S lower bound}} \leq \tilde{\kappa}^* = 96.17 \leq \underbrace{\kappa_2 + \frac{1-v_2}{\frac{1}{\kappa_1 - \kappa_2} + \frac{3v_2}{3\kappa_2 + 4\mu_2}}}_{\text{bulk modulus H/S upper bound}} = 102.38 \\
 35.43 = \underbrace{\mu_1 + \frac{v_2}{\frac{1}{\mu_2 - \mu_1} + \frac{6(1-v_2)(\kappa_1 + 2\mu_1)}{5\mu_1(3\kappa_1 + 4\mu_1)}}}_{\text{shear modulus H/S lower bound}} \leq \tilde{\mu}^* = 42.35 \leq \underbrace{\mu_2 + \frac{(1-v_2)}{\frac{1}{\mu_1 - \mu_2} + \frac{6v_2(\kappa_2 + 2\mu_2)}{5\mu_2(3\kappa_2 + 4\mu_2)}}}_{\text{shear modulus H/S upper bound}} = 45.64
 \end{aligned}
 \tag{21}$$

where κ_1, μ_1 and κ_2, μ_2 are the bulk and shear moduli for the matrix and particle phases. Despite the fact that the bounds are technically inapplicable for finite-sized samples, the computed results did fall within them.

Remark. A primary question is what other information can we extract from the average of the responses of many samples? In order to answer this question, we draw on some previous results found in References [11, 12].

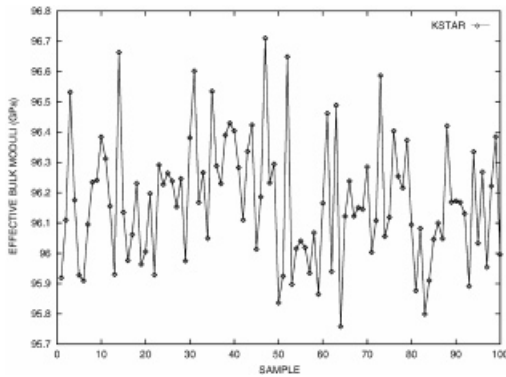


Figure 10. One-hundred samples: the bulk responses, κ^* , of a block with 20 randomly distributed Boron spheres embedded in an aluminium matrix. Each point represents the results of one test.

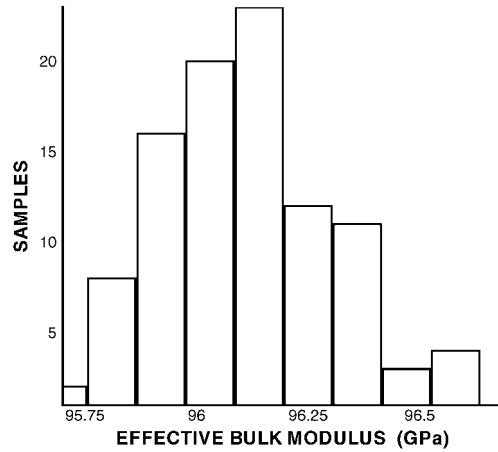


Figure 11. One-hundred samples: the corresponding histogram for the variations in the effective bulk responses, κ^* .

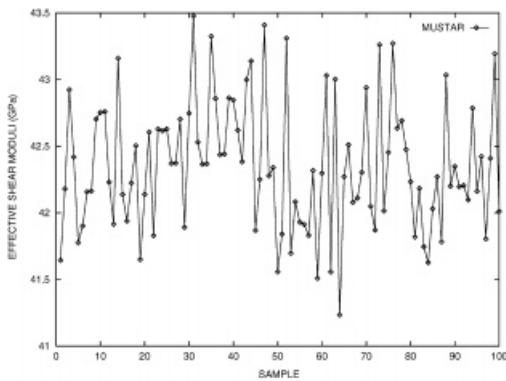


Figure 12. One-hundred samples: the shear responses, μ^* , of a block with 20 randomly distributed Boron spheres embedded in an aluminium matrix. Each point represents the results of one test.

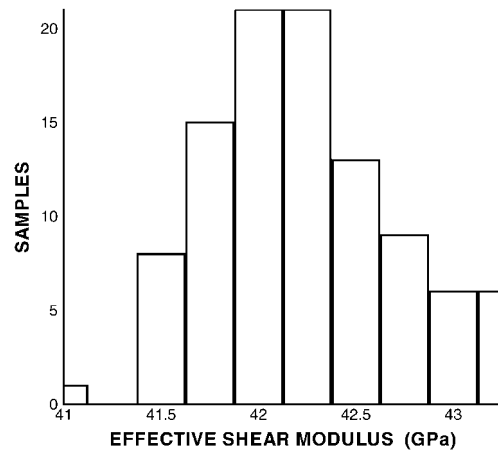


Figure 13. One-hundred samples: the corresponding histogram for the variations in the effective shear responses, μ^* .

5. A MINIMUM PRINCIPLE INTERPRETATION

Consider the following process for a sample of material with $\mathbf{u}|_{\partial\Omega} = \mathcal{E} \cdot \mathbf{x}$:

1. *Step 1*: Take a large sample, and cut it into N pieces, $\Omega = \bigcup_{K=1}^N \Omega_K$. The pieces do not have to be the same size or shape, although for illustration purposes it is convenient to take a uniform (regular) partitioning (Figure 18).

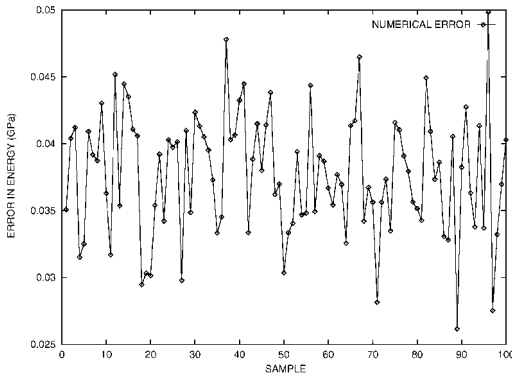


Figure 14. One-hundred samples: the numerical error monitor ξ of a block with 20 randomly distributed Boron spheres embedded in an aluminium matrix. Each point represents the results of one test.

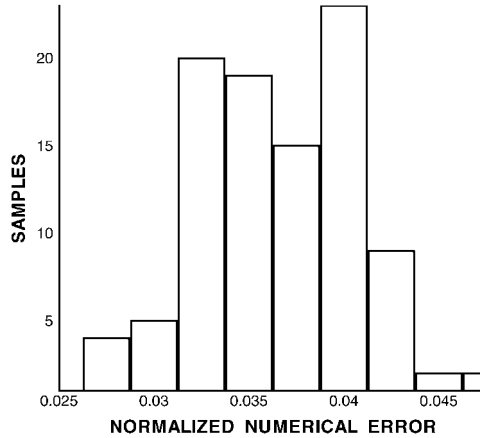


Figure 15. One-hundred samples: the corresponding histogram for the variations in the numerical error monitor ξ .

2. *Step 2:* Test each piece (solve the subdomain BVP) with the loading: $\mathbf{u}|_{\partial\Omega_K} = \mathcal{L} \cdot \mathbf{x}$. The function $\tilde{\mathbf{u}}_K$ is the solution to the BVP posed over subsample Ω_K .
3. *Step 3:* One is guaranteed the following properties:

$$\begin{aligned}
 \langle \tilde{\boldsymbol{\sigma}} \rangle_{\Omega_K} &\stackrel{\text{def}}{=} \tilde{\mathbb{E}}_K^* : \langle \tilde{\boldsymbol{\varepsilon}} \rangle_{\Omega_K}, & \tilde{\mathbb{E}}^* &\stackrel{\text{def}}{=} \sum_{K=1}^N \tilde{\mathbb{E}}_K^* \frac{|\Omega_K|}{|\Omega|} \\
 \|\mathbf{u} - \tilde{\mathbf{u}}\|_{E(\Omega)}^2 &= \mathcal{E} : (\tilde{\mathbb{E}}^* - \mathbb{E}^*) : \mathcal{E} |\Omega| \leq \mathcal{E} : (\tilde{\mathbb{E}}^* - \langle \mathbb{E}^{-1} \rangle_{\Omega}^{-1}) : \mathcal{E} |\Omega| \\
 \langle \mathbb{E}^{-1} \rangle_{\Omega}^{-1} &\leq \mathbb{E}^* \leq \tilde{\mathbb{E}}^* \leq \langle \mathbb{E} \rangle_{\Omega} \\
 \mathbf{u} &\stackrel{\text{def}}{=} \tilde{\mathbf{u}}_1|_{\tilde{\Omega}_1} + \tilde{\mathbf{u}}_2|_{\tilde{\Omega}_2} \cdots \tilde{\mathbf{u}}_N|_{\tilde{\Omega}_N}
 \end{aligned}
 \tag{22}$$

The same process can be done for the traction test loading case: $\mathbf{t}|_{\partial\Omega_K} = \mathcal{L} \cdot \mathbf{n}$ (see Appendix B). The effective process material ordering, line 3 in Box (22), has been derived by Huet [11]. The second line of Box (22), and generalizations to non-uniform loading, were developed in Reference [12]. The proofs, which are constructive, and illustrative of the main ideas, are provided next. They result from a direct manipulation of classical energy minimization principles.

5.1. A proof based on partitioning results

Consider a large sample whose domain consists of the union of many smaller domains, $\bigcup_{K=1}^N \Omega_K = \bar{\Omega}$, as depicted in Figure 18. The corresponding solution \mathbf{u} , denoted the globally

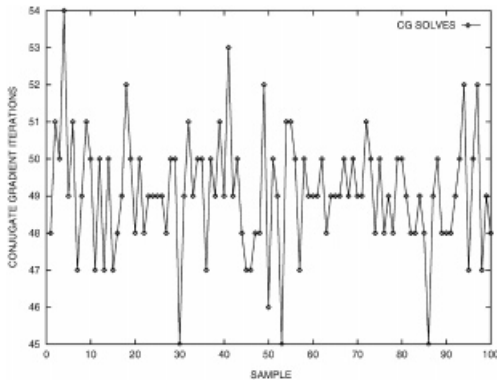


Figure 16. One-hundred samples: the conjugate gradient iterations of a block with 20 randomly distributed Boron spheres embedded in an aluminium matrix. Each point represents the results of one test.

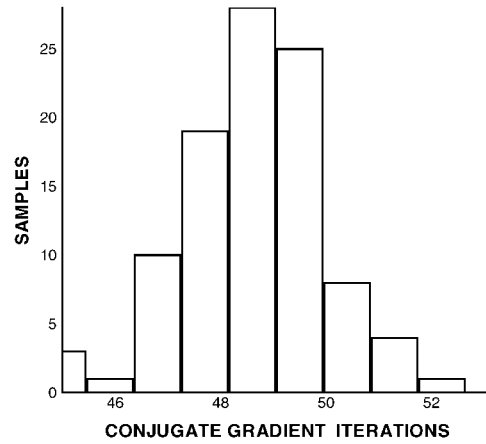


Figure 17. One-hundred samples: the corresponding histogram for the variations in conjugate gradient iterations needed for a solution.

Table III. Results of 100 material tests for randomly distributed particulate microstructures (20 spheres). We note that for a zero starting guess for the iterative solver, the average number of CG-iterations was 55, therefore using the initial Voigt ($\mathbf{u} = \mathcal{E} \cdot \mathbf{x}$) guess saved approximately 12 per cent of the computational solution effort. See Appendix C for more details.

Quantity	Average	Standard dev.	Max–Min
$\int_{\Omega} \nabla \mathbf{u} : \mathbb{E} : \nabla \mathbf{u} \, d\Omega$ (GPa)	0.001373	7.4×10^{-6}	3.6×10^{-5}
κ^* (GPa)	96.171	0.2025	0.950
μ^* (GPa)	42.350	0.4798	2.250
ξ	0.0376	0.0045	0.024
CG-ITER (iterations)	49.079	1.5790	9

exact solution, is characterized by the following variational boundary value problem:

$$\begin{aligned}
 &\text{Find } \mathbf{u} \in \mathbf{H}^1(\Omega), \mathbf{u}|_{\Gamma_u} = \mathbf{d}, \text{ such that} \\
 &\int_{\Omega} \nabla \mathbf{v} : \mathbb{E} : \nabla \mathbf{u} \, d\Omega = \int_{\Omega} \mathbf{f} \cdot \mathbf{v} \, d\Omega + \int_{\Gamma_t} \mathbf{t} \cdot \mathbf{v} \, dA \quad \forall \mathbf{v} \in \mathbf{H}^1(\Omega), \mathbf{v}|_{\Gamma_u} = \mathbf{0}
 \end{aligned}
 \tag{23}$$

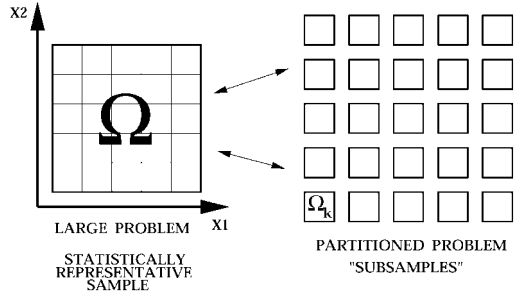


Figure 18. The idea of partitioning a sample into smaller samples or equivalently combining smaller samples into a larger sample.

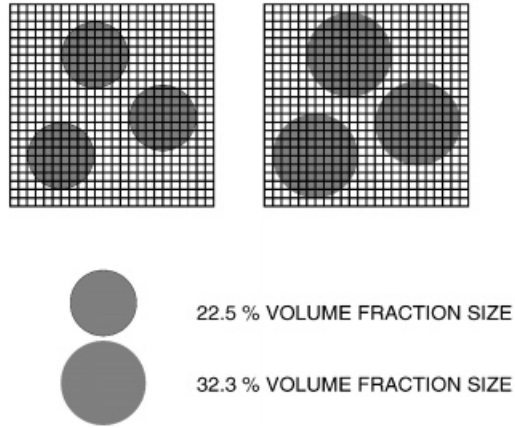


Figure 19. A comparison of relative sizes of particles occupying approximately 22 per cent ($\zeta=0.75$) and 32 per cent ($\zeta=0.85$) volume fraction.

Specific choices for \mathbf{d} , \mathbf{t} and \mathbf{f} will be given momentarily. Now consider the boundary of an individual subdomain Ω_K , as $\partial\Omega_K$, $1 \leq K \leq N$ (N is the total number of subdomains)

$$\begin{aligned}
 &\text{Find } \tilde{\mathbf{u}}_K \in \mathbf{H}^1(\Omega_K), \tilde{\mathbf{u}}_K|_{\partial\Omega_K \cap (\Omega \cup \Gamma_u)} = \mathbf{U} \in \mathbf{H}^1(\Omega), \text{ such that} \\
 &\int_{\Omega_K} \nabla \mathbf{v}_K : \tilde{\boldsymbol{\sigma}}_K \, d\Omega = \int_{\Omega_K} \mathbf{f} \cdot \mathbf{v}_K \, d\Omega + \int_{\partial\Omega_K \cap \Gamma_t} \mathbf{t} \cdot \mathbf{v}_K \, dA \\
 &\forall \mathbf{v}_K \in \mathbf{H}^1(\Omega_K), \mathbf{v}_K|_{\partial\Omega_K \cap (\Omega \cup \Gamma_u)} = 0
 \end{aligned}
 \tag{24}$$

A specific choice for \mathbf{U} will also be given momentarily. The individual subdomain solutions form an approximate solution to the globally exact problem, \mathbf{u} . This approximate solution is constructed by a direct assembly process

$$\tilde{\mathbf{u}} \stackrel{\text{def}}{=} \tilde{\mathbf{u}}_1|_{\tilde{\Omega}_1} + \dots + \tilde{\mathbf{u}}_N|_{\tilde{\Omega}_N}
 \tag{25}$$

The approximate displacement field is continuous, however, the approximate traction field is usually discontinuous.

5.1.1. *Relation to the material tests.* We recall that for any admissible \mathbf{w} , we have from the *principle of minimum potential energy* (PMPE), $\|\mathbf{u} - \mathbf{w}\|_{E(\Omega)}^2 = 2\mathcal{J}(\mathbf{w}) - 2\mathcal{J}(\mathbf{u})$,

we obtain

$$\|\mathbf{u} - \mathbf{w}\|_{E(\Omega)}^2 = 2(\mathcal{J}(\mathbf{w}) - \mathcal{J}(\mathbf{u})) \Rightarrow \mathcal{J}(\mathbf{u}) = \mathcal{J}(\mathbf{w}) - \frac{1}{2}\|\mathbf{u} - \mathbf{w}\|_{E(\Omega)}^2 \tag{26}$$

The critical observation is to now consider choosing $\mathbf{w} = \mathbf{U} \stackrel{\text{def}}{=} \mathcal{E} \cdot \mathbf{x}$ in Box (24). Therefore $\tilde{\mathbf{u}}$, as defined in Box (25), is also kinematically admissible, we have by direct expansion

$$\|\mathbf{u} - \tilde{\mathbf{u}}\|_{E(\Omega)}^2 = 2(\mathcal{J}(\tilde{\mathbf{u}}) - \mathcal{J}(\mathbf{u})) = 2(\mathcal{J}(\tilde{\mathbf{u}}) - \mathcal{J}(\mathbf{w})) + \|\mathbf{u} - \mathbf{w}\|_{E(\Omega)}^2 \tag{27}$$

Since $\tilde{\mathbf{u}}_k$ is a solution to a subdomain boundary value problem posed over Ω_k , it minimizes the corresponding subdomain potential energy function $\mathcal{J}_k(\cdot)$. Therefore,

$$\mathcal{J}(\mathbf{w}) = \sum_{K=1}^N \mathcal{J}_K(\mathbf{w}) \geq \sum_{K=1}^N \mathcal{J}_K(\tilde{\mathbf{u}}_K) = \mathcal{J}(\tilde{\mathbf{u}}) \tag{28}$$

Consequently,

$$\|\mathbf{u} - \tilde{\mathbf{u}}\|_{E(\Omega)}^2 = \underbrace{2(\mathcal{J}(\tilde{\mathbf{u}}) - \mathcal{J}(\mathbf{w}))}_{\text{negative}} + \|\mathbf{u} - \mathbf{w}\|_{E(\Omega)}^2 \tag{29}$$

By direct expansion we have

$$\|\mathbf{u} - \mathbf{w}\|_{E(\Omega)}^2 = \mathcal{E} : (\langle \mathbb{E} \rangle - \mathbb{E}^*) : \mathcal{E} |\Omega| \leq \mathcal{E} : (\langle \mathbb{E} \rangle - \langle \mathbb{E}^{-1} \rangle^{-1}) : \mathcal{E} |\Omega| \tag{30}$$

We have by definition

$2\mathcal{J}(\mathbf{u}) = \mathcal{E} : \mathbb{E}^* : \mathcal{E} \Omega $ $2\mathcal{J}_K(\tilde{\mathbf{u}}) = \mathcal{E} : \tilde{\mathbb{E}}_K^* : \mathcal{E} \Omega_K \Rightarrow 2\mathcal{J}(\tilde{\mathbf{u}}) = \mathcal{E} : \tilde{\mathbb{E}}^* : \mathcal{E} \Omega $ $2\mathcal{J}(\mathbf{w}) = \mathcal{E} : \langle \mathbb{E} \rangle : \mathcal{E} \Omega $	\tag{31}
---	----------

By direct substitution this completes the first of the assertions in Box (22). For traction tests, the procedure is similar, and is discussed in Appendix B for completeness. We can directly interpret the testing of many smaller samples as simply the partitioning of a very large one which we cannot easily test (Figure 18). Therefore, for displacement tests, the averaged effective responses generated will always bound the response of the very large sample from above. Therefore, the average of the 100 sample tests provide us with tighter upper bounds on the response of a very large sample. Therefore, by the previously proven results in Box (22), the Reuss–Voigt bounds in Box (20) are tightened by the following factors:

$\frac{96.17 - 91.37}{111.79 - 91.37} = 0.2747$ $\frac{42.35 - 30.76}{57.68 - 30.76} = 0.4305$	\tag{32}
--	----------

As shown in Appendix B for traction tests the testing of the smaller samples will bound the response of the very large sample from below.

5.1.2. *Isolating the subsampling error/numerical error orthogonality.* According to the results in Box (22), we have the following normalized estimate:

$$\frac{\|\mathbf{u} - \tilde{\mathbf{u}}\|_{\tilde{E}(\Omega)}^2}{\mathcal{E} : \langle \mathbb{E} \rangle_{\Omega} : \mathcal{E} |\Omega|} = \frac{\mathcal{E} : (\tilde{\mathbb{E}}^* - \mathbb{E}^*) : \mathcal{E} |\Omega|}{\mathcal{E} : \langle \mathbb{E} \rangle_{\Omega} : \mathcal{E} |\Omega|} \leq \frac{\mathcal{E} : (\tilde{\mathbb{E}}^* - \langle \mathbb{E}^{-1} \rangle_{\Omega}^{-1}) : \mathcal{E} |\Omega|}{\mathcal{E} : \langle \mathbb{E} \rangle_{\Omega} : \mathcal{E} |\Omega|} \tag{33}$$

where, since we have used displacement controlled tests, we have used the Voigt material’s energy, which corresponds to assuming a constant strain throughout the material equal to \mathcal{E} , to normalize the results.

It is important to note that the numerical error, which is implicitly included in the estimate in Equation (33), is orthogonal to the ‘partitioning’ or ‘subsampling’ error. In other words, while the numerical error is known, it can be directly filtered out of the sampling error estimates. To see this, consider that the boundary value formulations in Boxes (23) and (24) directly imply, for any type of loading

$$\int_{\Omega} \nabla \mathbf{v} : \mathbb{E} : \nabla (\mathbf{u} - \tilde{\mathbf{u}}) \, d\Omega = 0, \quad \forall \mathbf{v} \in \mathbf{H}^1(\Omega), \mathbf{v}|_{\Omega \cap \partial\Omega_K} = \mathbf{0}, \quad K = 1, 2, 3, \dots, N \tag{34}$$

This directly implies that

$$\int_{\Omega} \nabla (\tilde{\mathbf{u}} - \tilde{\mathbf{u}}^h) : \mathbb{E} : \nabla (\mathbf{u} - \tilde{\mathbf{u}}) \, d\Omega = 0 \tag{35}$$

Therefore,

$$\begin{aligned} \|\mathbf{u} - \tilde{\mathbf{u}}^h\|_{\tilde{E}(\Omega)}^2 &= \|\mathbf{u} - \tilde{\mathbf{u}} + \tilde{\mathbf{u}} - \tilde{\mathbf{u}}^h\|_{\tilde{E}(\Omega)}^2 \\ &= \int_{\Omega} \nabla (\mathbf{u} - \tilde{\mathbf{u}}) : \mathbb{E} : \nabla (\mathbf{u} - \tilde{\mathbf{u}}) \, d\Omega - 2 \underbrace{\int_{\Omega} \nabla (\tilde{\mathbf{u}} - \tilde{\mathbf{u}}^h) : \mathbb{E} : \nabla (\mathbf{u} - \tilde{\mathbf{u}}) \, d\Omega}_{=0 \text{ by the above}} \\ &\quad + \int_{\Omega} \nabla (\tilde{\mathbf{u}} - \tilde{\mathbf{u}}^h) : \mathbb{E} : \nabla (\tilde{\mathbf{u}} - \tilde{\mathbf{u}}^h) \, d\Omega \\ &= \|\mathbf{u} - \tilde{\mathbf{u}}\|_{\tilde{E}(\Omega)}^2 + \|\tilde{\mathbf{u}} - \tilde{\mathbf{u}}^h\|_{\tilde{E}(\Omega)}^2 \end{aligned} \tag{36}$$

Under the special case that $\mathbf{U} \stackrel{\text{def}}{=} \mathcal{E} \cdot \mathbf{x}$, we have the following orthogonal decomposition of sampling and numerical error:

$$\underbrace{\mathcal{E} : (\tilde{\mathbb{E}}^{*,h} - \mathbb{E}^*) : \mathcal{E} |\Omega|}_{\|\mathbf{u} - \tilde{\mathbf{u}}^h\|_{\tilde{E}(\Omega)}^2} = \underbrace{\mathcal{E} : (\tilde{\mathbb{E}}^* - \mathbb{E}^*) : \mathcal{E} |\Omega|}_{\|\mathbf{u} - \tilde{\mathbf{u}}\|_{\tilde{E}(\Omega)}^2} + \underbrace{\sum_{K=1}^N \|\tilde{\mathbf{u}}_K^h - \tilde{\mathbf{u}}_K\|_{\tilde{E}(\Omega)}^2}_{\mathcal{E} : (\tilde{\mathbb{E}}^{*,h} - \mathbb{E}^*) : \mathcal{E} |\Omega|} \tag{37}$$

where

$$\langle \tilde{\boldsymbol{\sigma}}^h \rangle_{\Omega_K} \stackrel{\text{def}}{=} \tilde{\mathbb{E}}_K^{*,h} : \langle \tilde{\boldsymbol{\varepsilon}}^h \rangle_{\Omega_K}, \quad \tilde{\mathbb{E}}^{*,h} \stackrel{\text{def}}{=} \sum_{K=1}^N \tilde{\mathbb{E}}_K^{*,h} \frac{|\Omega_K|}{|\Omega|} \tag{38}$$

Therefore, the expression in Equation (37) indicates that the estimates made on the effective response is an orthogonal sum of both the numerical and sampling error. Therefore, one can isolate either the numerical or sampling error, if the other is known, or estimated, by simply subtracting it from the total expression (the left-hand side of Equation (37)). Therefore, for example, approximating the numerical error by the error monitor, ξ , we have

$$\begin{aligned} \text{Subsampling error} &= \frac{\mathcal{E} : (\tilde{\mathbb{E}}^* - \langle \mathbb{E}^{-1} \rangle_{\Omega}^{-1}) : \mathcal{E} |\Omega|}{\mathcal{E} : \langle \mathbb{E} \rangle_{\Omega} : \mathcal{E} |\Omega|} - \xi \\ &= 0.1073 - 0.0376 = 0.0697 \end{aligned} \tag{39}$$

This quantity represents the isolated error in the internal fields induced by the partitioning or subsampling only. More general theoretical relationships between sampling and numerical error can be found in Reference [12].

5.2. Some remarks on higher volume fractions

We repeated the 100 sample tests procedure for samples containing significantly higher volume fraction, approximately 32 per cent. Unlike fibre-reinforced composites, which can contain well over 50 per cent volume fraction of fibers, particulate composites usually contain no more than approximately 25 per cent volume fraction of particulates. Particulate volume fractions over 15 per cent are already high in three dimensions. For the relevant examples, 22 per cent particulate volume fraction in three dimensions corresponds roughly to 44 per cent in two dimensions, while 32 per cent in three dimension corresponds roughly to 57 per cent in two dimensions. Cross-sections of these volume fractions are depicted in Figure 19. The results for the 32 per cent case are tabulated in Table IV. The averages for the effective properties of the sample were

$$\begin{aligned} 99.04 &= \langle \kappa^{-1} \rangle_{\Omega}^{-1} \leq \tilde{\kappa}^* = 106.83 \leq \langle \kappa \rangle_{\Omega} = 126.99 \\ 34.39 &= \langle \mu^{-1} \rangle_{\Omega}^{-1} \leq \tilde{\mu}^* = 52.63 \leq \langle \mu \rangle_{\Omega} = 72.38 \end{aligned} \tag{40}$$

where $\tilde{\kappa}^*$ and $\tilde{\mu}^*$ are the averaged quantities from the 100 tests, and where the lower and upper bounds are, respectively, the classical Reuss [7] and Voigt [8] bounds. The Reuss–Voigt bounds in Box (40) are tightened by the following factors:

$$\begin{aligned} \frac{106.831 - 99.043}{126.999 - 99.043} &= 0.2785 \\ \frac{52.635 - 34.395}{72.385 - 34.395} &= 0.4801 \end{aligned} \tag{41}$$

Table IV. Results of 100 material tests for randomly distributed particulate micro-structures (20 spheres, $\zeta = 0.85$, approximately 32 per cent volume fraction).

Subdomain quantity	Aver.	7 Stan. Dev.	Max–Min
W (GPa)	0.001593	9.11×10^{-6}	5×10^{-5}
κ^* (GPa)	106.831	0.2505	1.350
μ^* (GPa)	52.635	0.5876	3.095
ζ	0.0523	0.0044	0.0255
CG-ITER (iterations)	48.950	1.716	8

The error estimate in this case is

$$\begin{aligned} \text{Subsampling error} &\approx \frac{\mathcal{E} : (\tilde{\mathbb{E}}^* - \langle \mathbb{E}^{-1} \rangle_{\Omega}^{-1}) : \mathcal{E} |\Omega|}{\mathcal{E} : \langle \mathbb{E} \rangle_{\Omega} : \mathcal{E} |\Omega|} - \zeta \\ &= 0.1436 - 0.05231 = 0.09129 \end{aligned} \tag{42}$$

which is approximately 2 per cent higher error estimate than the case of 22 per cent particulate volume fraction. Intuitively, one would expect such a result, since the particles interact more at such a high volume fraction (Figure 19). In other words, they ‘feel’ the presence of the other particles more at higher volume fractions than at lower volume fractions. As before, we also compared the computed results to Hashin–Shtrikman bounds [9, 10] which are, strictly speaking, *only applicable* to asymptotic cases of an infinite (sample length)/(particulate length) ratio, and purely isotropic macroscopic responses

$$103.378 = \underbrace{\kappa_1 + \frac{v_2}{\frac{1}{\kappa_2 - \kappa_1} + \frac{3(1-v_2)}{3\kappa_1 + 4\mu_1}}}_{\text{bulk modulus H/S lower bound}} \leq \tilde{\kappa}^* = 106.831 \leq \underbrace{\kappa_2 + \frac{1-v_2}{\frac{1}{\kappa_1 - \kappa_2} + \frac{3v_2}{3\kappa_2 + 4\mu_2}}}_{\text{bulk modulus H/S upper bound}} = 114.671$$

$$41.624 = \underbrace{\mu_1 + \frac{v_2}{\frac{1}{\mu_2 - \mu_1} + \frac{6(1-v_2)(\kappa_1 + 2\mu_1)}{5\mu_1(3\kappa_1 + 4\mu_1)}}}_{\text{shear modulus H/S lower bound}} \leq \tilde{\mu}^* = 52.635 \leq \underbrace{\mu_2 + \frac{(1-v_2)}{\frac{1}{\mu_1 - \mu_2} + \frac{6v_2(\kappa_2 + 2\mu_2)}{5\mu_2(3\kappa_2 + 4\mu_2)}}}_{\text{shear modulus H/S upper bound}} = 56.437$$

(43)

6. CONCLUDING COMMENTS AND FUTURE WORK

Beyond a certain threshold, it is simply impossible to obtain any more information by testing samples of a certain size. As we have shown the reason for the inability for obtaining

Table V. Results of material tests for randomly distributed particulate microstructures for 100 ($\zeta = 0.75$, approximately 22 per cent) samples of 40 and 60 particles per sample.

Part	d/L	Dof	Quantity	Aver.	Stan. Dev.	Max–Min
40	0.2193	98 304	W (GPa)	0.0013617	5.0998×10^{-6}	2.35×10^{-5}
40	0.2193	98 304	κ^* (GPa)	95.7900	0.1413	0.6600
40	0.2193	98 304	μ^* (GPa)	41.6407	0.3245	1.590
40	0.2193	98 304	CG-ITER	60.3200	1.6302	7
60	0.1916	139 968	W (GPa)	0.0013586	4.3963×10^{-6}	2.25×10^{-5}
60	0.1916	139 968	κ^* (GPa)	95.6820	0.1197	0.6214
60	0.1916	139 968	μ^* (GPa)	41.4621	0.2801	1.503
60	0.1916	139 968	CG-ITER	66.500	1.9974	10

anymore information is the fact that the testing conditions are uniform on the ‘subsamples’. This idealization is valid only for an infinitely large sample. However, suppose we increase the number of particles per subsample even further, from 20 to say 40 then 60, each time performing the 100 tests procedure. With this information one could then possibly extrapolate to a (giant) sample limit. The results for the 40 and 60 particle cases are shown in Table V for 22 per cent Boron volume fraction. Using these results, along with the 20 particle per sample tests, we have the following curve fits:

$$\begin{aligned}
 W &= 0.0013205 + 0.0001895 \frac{d}{L}, \quad R^2 = 0.9997 \\
 \kappa^* &= 94.527 + 5.909 \frac{d}{L}, \quad R^2 = 0.986 \\
 \mu^* &= 39.345 + 10.775 \frac{d}{L}, \quad R^2 = 0.986
 \end{aligned}
 \tag{44}$$

where L is the sample size, d is the diameter of the particles. Thus as $d/L \rightarrow 0$, we obtain an estimates of $W = 0.0013205$, $\kappa^* = 94.527$ and $\mu^* = 39.345$ GPa as the asymptotic energy, effective bulk modulus, and effective shear modulus, respectively. Indeed, judging from the degree of accuracy of the curve-fit, ($R^2 = 1.0$ is perfect) the data appears to be reliable. The slightly less, although still quite accurate, reliability (regression values of $R^2 = 0.98$) of the effective responses, κ^* and μ^* , is attributed to the fact that absolute perfect isotropy is impossible to achieve with finite-sized samples. In other words, the extrapolations using various samples exhibit slight isotropic inconsistencies. However, the energy W , has no built-in assumptions whatsoever, thus leading to the nearly perfect curve-fit. Further development and extension of the multiple sample testing techniques, in conjunction with the mentioned extrapolation technique, is under current investigation by the authors.

APPENDIX A: THE FINITE ELEMENT METHOD

The essential idea in the finite element method is to select a finite-dimensional subspace approximation of the true solution and form the following variational boundary problem:

$$\boxed{
 \begin{aligned}
 &\text{Find } \mathbf{u}^h \in \mathbf{H}_u^h(\Omega) \subset \mathbf{H}^1(\Omega), \mathbf{u}^h|_{\Gamma_u} = \mathbf{d}, \text{ such that} \\
 &\underbrace{\int_{\Omega} \nabla \mathbf{v}^h : \mathbb{E} : \nabla \mathbf{u}^h \, d\Omega}_{\mathcal{B}(\mathbf{u}^h, \mathbf{v}^h)} = \underbrace{\int_{\Omega} \mathbf{f} \cdot \mathbf{v}^h \, d\Omega + \int_{\Gamma_t} \mathbf{t} \cdot \mathbf{v}^h \, dA}_{\mathcal{F}(\mathbf{v}^h)} \\
 &\forall \mathbf{v}^h \in \mathbf{H}_v^h(\Omega) \subset \mathbf{H}^1(\Omega), \mathbf{v}^h|_{\Gamma_u} = \mathbf{0}
 \end{aligned}
 } \tag{A1}$$

The critical point is that $\mathbf{H}_u^h(\Omega), \mathbf{H}_v^h(\Omega) \subset \mathbf{H}^1(\Omega)$. This ‘inner’ approximation allows the development of straightforward subspace error estimates. In most cases $\mathbf{H}_u^h(\Omega)$ and $\mathbf{H}_v^h(\Omega)$ coincide.

Under standard assumptions the fundamental *a priori* error estimate for the finite element method is (see for example Reference [13]):

$$\|\mathbf{u} - \mathbf{u}^h\|_{E(\Omega)} \leq \mathcal{C}(\mathbf{u}, p) h^{\min(r-1, p)} \stackrel{\text{def}}{=} w \tag{A2}$$

where p is the (complete) polynomial order of the finite element method used, s is the regularity of the exact solution, \mathcal{C} is a global constant dependent on the exact solution and the polynomial approximation. \mathcal{C} is independent of h , the maximum element diameter. Related forms of this estimate holds locally, but with constants that are element dependent.

For any $\mathbf{z}^h \in \mathbf{H}^s(\Omega) \subset \mathbf{H}^r(\Omega)$

$$\|\mathbf{u} - \mathbf{z}^h\|_{H^s(\Omega)} \leq Ch^w \|\mathbf{u}\|_{H^r(\Omega)}, \quad w = \min(p + 1 - s, r - s) \tag{A3}$$

where h is the largest element diameter. We have

$$\boxed{
 \begin{aligned}
 &\mathcal{B}(\mathbf{u}, \mathbf{v}) = \mathcal{F}(\mathbf{v}) \quad \forall \mathbf{v} \in \mathbf{H}^1(\Omega) \\
 &\mathcal{B}(\mathbf{u}^h, \mathbf{v}^h) = \mathcal{F}(\mathbf{v}^h) \quad \forall \mathbf{v}^h \in \mathbf{H}_v^h(\Omega) \subset \mathbf{H}^1(\Omega)
 \end{aligned}
 } \tag{A4}$$

implying a Galerkin orthogonality property of inner approximations’:

$$\mathcal{B}(\mathbf{u} - \mathbf{u}^h, \mathbf{v}^h) = 0 \quad \forall \mathbf{v}^h \in \mathbf{H}_v^h(\Omega) \subset \mathbf{H}^1(\Omega) \tag{A5}$$

The error is defined by

$$\mathbf{e}^h \stackrel{\text{def}}{=} \mathbf{u} - \mathbf{u}^h \tag{A6}$$

Therefore any member of the subspace can be represented by

$$\mathbf{e}^h - \mathbf{v} = \mathbf{u} - \mathbf{u}^h - \mathbf{v} = \mathbf{u} - \mathbf{z}^h \tag{A7}$$

Using this representation we have

$$\begin{aligned} \mathcal{B}(\mathbf{e}^h - \mathbf{v}, \mathbf{e}^h - \mathbf{v}) &= \mathcal{B}(\mathbf{e}, \mathbf{e}) - \underbrace{2\mathcal{B}(\mathbf{e}^h, \mathbf{v})}_{=0} + \mathcal{B}(\mathbf{v}, \mathbf{v}) \Rightarrow \mathcal{B}(\mathbf{u} - \mathbf{u}^h, \mathbf{u} - \mathbf{u}^h) \\ &\leq \mathcal{B}(\mathbf{u} - \mathbf{z}^h, \mathbf{u} - \mathbf{z}^h) \end{aligned} \tag{A8}$$

We recall that \mathbb{E} is bounded in the following sense:

$$a_+ \boldsymbol{\varepsilon} : \boldsymbol{\varepsilon} \geq \boldsymbol{\varepsilon} : \mathbb{E}(x) : \boldsymbol{\varepsilon} \geq a_- \boldsymbol{\varepsilon} : \boldsymbol{\varepsilon} \quad \forall \boldsymbol{\varepsilon} \in \mathbb{R}^{3 \times 3}, \quad \boldsymbol{\varepsilon} = \boldsymbol{\varepsilon}^T, \quad \infty > a_-, a_+ > 0 \tag{A9}$$

With this we finally have

$$\begin{aligned} \|\mathbf{u} - \mathbf{u}^h\|_{E(\Omega)}^2 &\leq \frac{1}{a_-} \mathcal{B}(\mathbf{e}^h, \mathbf{e}^h) \\ &\leq \frac{1}{a_-} \mathcal{B}(\mathbf{u} - \mathbf{z}^h, \mathbf{u} - \mathbf{z}^h) \\ &\leq \frac{a_+}{a_-} \|\mathbf{u} - \mathbf{z}^h\|_{E(\Omega)}^2 \\ &\leq Ch^r \|\mathbf{u}\|_{E(\Omega)}^2 \end{aligned} \tag{A10}$$

This result holds locally as well, but with the constant being different for each element.

APPENDIX B: PARTITIONING AND TRACTION TEST CASES

Suppose we repeat the partitioning process for the applied internal traction case. Employing the *principle of complementary potential energy*, we obtain for the test loading $\mathbf{t}|_{\partial\Omega_K} = \mathcal{L} \cdot \mathbf{n}$, with $\boldsymbol{\gamma} = \mathcal{L}$ (a statically admissible trial field)

$$\begin{aligned} \|\boldsymbol{\sigma} - \tilde{\boldsymbol{\sigma}}\|_{E^{-1}(\Omega)}^2 &= 2(\mathcal{H}(\tilde{\boldsymbol{\sigma}}) - \mathcal{H}(\boldsymbol{\sigma})) \\ &= \underbrace{2(\mathcal{H}(\tilde{\boldsymbol{\sigma}}) - \mathcal{H}(\boldsymbol{\gamma}))}_{\text{negative}} + \|\boldsymbol{\sigma} - \boldsymbol{\gamma}\|_{E^{-1}(\Omega)}^2 \end{aligned} \tag{B1}$$

where

$$0 \leq \|\boldsymbol{\sigma} - \tilde{\boldsymbol{\sigma}}\|_{E^{-1}(\Omega)}^2 \stackrel{\text{def}}{=} \int_{\Omega} (\boldsymbol{\sigma} - \tilde{\boldsymbol{\sigma}}) : \mathbb{E}^{-1} : (\boldsymbol{\sigma} - \tilde{\boldsymbol{\sigma}}) \, d\Omega \tag{B2}$$

and where $\mathcal{H}(\boldsymbol{\sigma}) \stackrel{\text{def}}{=} \frac{1}{2} \int_{\Omega} \boldsymbol{\sigma} : \mathbb{E}^{-1} : \boldsymbol{\sigma} \, d\Omega - \int_{\Gamma_u} \boldsymbol{\sigma} \cdot \mathbf{n} \cdot \mathbf{d} \, dA$, $\tilde{\boldsymbol{\sigma}}$ being the stress field produced by solving each subsample problem with the uniform stress boundary conditions and forming

$$\tilde{\boldsymbol{\sigma}} \stackrel{\text{def}}{=} \tilde{\boldsymbol{\sigma}}_1|_{\tilde{\Omega}_1} + \tilde{\boldsymbol{\sigma}}_2|_{\tilde{\Omega}_2} \dots \tilde{\boldsymbol{\sigma}}_N|_{\tilde{\Omega}_N} \tag{B3}$$

By direct expansion we have

$$\|\boldsymbol{\sigma} - \boldsymbol{\gamma}\|_{E^{-1}(\Omega)}^2 = \mathcal{L} : (\langle \mathbb{E}^{-1} \rangle - \mathbb{E}^{-1*}) : \mathcal{L} |\Omega| \leq \mathcal{L} : (\langle \mathbb{E}^{-1} \rangle - \langle \mathbb{E} \rangle^{-1}) : \mathcal{L} |\Omega| \tag{B4}$$

The complementary forms collapse to

$$\begin{aligned}
 2\mathcal{H}(\boldsymbol{\sigma}) &= \mathcal{L} : \mathbb{E}^{-1*} : \mathcal{L}|\Omega| \\
 2\mathcal{H}_K(\tilde{\boldsymbol{\sigma}}) &= \mathcal{L} : \tilde{\mathbb{E}}_K^{-1*} : \mathcal{L}|\Omega_K| \Rightarrow 2\mathcal{H}(\tilde{\boldsymbol{\sigma}}) = \mathcal{L} : \tilde{\mathbb{E}}^{-1*} : \mathcal{L}|\Omega| \\
 2\mathcal{H}(\boldsymbol{\gamma}) &= \mathcal{L} : \langle \mathbb{E}^{-1} \rangle : \mathcal{L}|\Omega|
 \end{aligned}
 \tag{B5}$$

where $\mathcal{H}_K(\cdot)$ is the subdomain complementary potential energy function for subdomain K . By direct substitution this yields

$$\begin{aligned}
 \langle \tilde{\boldsymbol{\epsilon}} \rangle_{\Omega_K} &= \tilde{\mathbb{E}}_K^{-1*} : \langle \tilde{\boldsymbol{\sigma}} \rangle_{\Omega_K} \quad \tilde{\mathbb{E}}^{-1*} \stackrel{\text{def}}{=} \sum_{K=1}^N \tilde{\mathbb{E}}_K^{-1*} \frac{|\Omega_K|}{|\Omega|} \\
 \|\boldsymbol{\sigma} - \tilde{\boldsymbol{\sigma}}\|_{E^{-1}(\Omega)}^2 &= \mathcal{L} : (\tilde{\mathbb{E}}^{-1*} - \mathbb{E}^{*-1}) : \mathcal{L}|\Omega| \\
 &\leq \mathcal{L} : (\tilde{\mathbb{E}}^{-1*} - \langle \mathbb{E} \rangle_{\Omega}^{-1}) : \mathcal{L}|\Omega| \\
 \langle \mathbb{E}^{-1} \rangle_{\Omega} &\geq \tilde{\mathbb{E}}^{-1*} \geq \mathbb{E}^{-1*} \geq \langle \mathbb{E} \rangle_{\Omega}^{-1} \\
 \tilde{\boldsymbol{\sigma}} &\stackrel{\text{def}}{=} \tilde{\boldsymbol{\sigma}}_1|_{\tilde{\Omega}_1} + \tilde{\boldsymbol{\sigma}}_2|_{\tilde{\Omega}_2} \dots \tilde{\boldsymbol{\sigma}}_N|_{\tilde{\Omega}_N}
 \end{aligned}
 \tag{B6}$$

The second line of Box B6, and generalizations to non-uniform loading, were developed in Reference [12]. The fourth line has been derived in Reference [11] by other means.

B.1. Consequences/difficulties with traction tests

If the sample were an RVE, we have $\mathbb{E}^{-1*} = \mathbb{E}^{*-1}$, then the preceding analysis yields the following two sided ordering of approximate effective materials:

$$\langle \mathbb{E}^{-1} \rangle_{\Omega}^{-1} \leq (\tilde{\mathbb{E}}^{-1*})^{-1} \leq \mathbb{E}^* \leq \tilde{\mathbb{E}}^* \leq \langle \mathbb{E} \rangle_{\Omega}
 \tag{B7}$$

We emphasize that $\mathbb{E}^{-1*} = \mathbb{E}^{*-1}$ is an assumption, which may not be true for a finite-sized sample. Therefore, in theory, under the RVE assumption, traction tests form lower bounds on the effective responses. However, traction tests pose great difficulties, which are as follows:

1. Numerically pure traction boundary data cause rigid motions (singular FEM stiffness matrices).
2. The FEM is a method based upon generating kinematically admissible solutions $\tilde{\boldsymbol{\sigma}}$. The traction tests result is based upon the assumption that statically admissible trial field are generated. Statically admissible fields cannot be achieved by a standard FEM approach.
3. True laboratory tests specifying the force on a sample are far more difficult than specifying the displacements.

APPENDIX C. ITERATIVE KRYLOV SOLVERS AS MICROSTRUCTURAL ‘CORRECTORS’

Since the operation counts to factor and solve an $n \times n$ discrete algebraic system is $\mathcal{O}(n^3)$ with Gaussian elimination, iterative solvers, such as the conjugate gradient method (CG), are preferred when the systems are very large. This choice is made under the premise that if perfect numerical algebra is performed, the CG method, which involves a matrix/vector multiplication costing $2n^2$ operation counts per iteration, is convergent in less than n iterations. The CG method is commonly used as an iterative solution method for algebraic systems such as $[\mathbf{K}]\{\mathbf{u}\} = [\mathbf{B}]$. Here $[\mathbf{K}]$ is a symmetric positive-definite $n \times n$ (stiffness) matrix, $\{\mathbf{u}\}$ is the $n \times 1$ solution vector, and $[\mathbf{B}]$ is the $n \times 1$ right-hand side (load vector). The basic approach is to minimize a corresponding quadratic function, or a potential $\Psi \stackrel{\text{def}}{=} \frac{1}{2}\{\mathbf{u}\}^T[\mathbf{K}]\{\mathbf{u}\} - \{\mathbf{u}\}^T[\mathbf{B}]$. From basic calculus we have $\nabla\Psi \stackrel{\text{def}}{=} (\partial\Psi/\partial u_1, \partial\Psi/\partial u_2, \dots, \partial\Psi/\partial u_n)^T = \mathbf{0} \Rightarrow [\mathbf{K}]\{\mathbf{u}\} - [\mathbf{B}] = \mathbf{0}$. Therefore, the minimizer of the potential Ψ is also the solution to the discrete system. For the various characteristics of the method see Reference [14].

For micromechanics problems, one important feature of iterative solvers, such as the CG method, is the fact that since they are based on successive updates of a starting guess solution vector. Consequently, they can be given a head start by a good solution guess, for example, provided by an inexpensive analytical approximation solution. For example, in a micromechanical context, the conjugate gradient (CG) method can be interpreted as making fine scale (high-frequency) corrections with each iteration. Importantly, one should use inexpensive approximate solutions as initial guesses for the iterative solver. This greatly enhances the effectiveness of the CG searches for this class of problems. A well-known fact, with regard to iterative solvers is the fact that they are quite adept at capturing high-frequency responses. However, they typically may require many iterations to capture ‘long-wave’ modes. For a discussion see Reference [15]. In other words, a starting vector that captures *a priori* the ‘long-wave’ components of the solution is of great advantage.

We assume that either of the two classical boundary conditions that satisfy Hill’s conditions hold: (1) $\mathbf{u}|_{\partial\Omega} = \mathcal{E} \cdot \mathbf{x} \Rightarrow \langle \boldsymbol{\varepsilon} \rangle_{\Omega} = \mathcal{E}$ and (2) $\mathbf{t}|_{\partial\Omega} = \mathcal{L} \cdot \mathbf{n} \Rightarrow \langle \boldsymbol{\sigma} \rangle_{\Omega} = \mathcal{L}$. The classical assumptions of Voigt [8] (uniform strain) and Reuss [7] (uniform stress) produce the following:

$$\begin{aligned} \text{Voigt: } \boldsymbol{\varepsilon} = \text{Constant} &\Rightarrow \langle \boldsymbol{\sigma} \rangle_{\Omega} = \langle \mathbb{E} : \boldsymbol{\varepsilon} \rangle_{\Omega} = \langle \mathbb{E} \rangle_{\Omega} : \langle \boldsymbol{\varepsilon} \rangle_{\Omega} \\ \text{Reuss: } \boldsymbol{\sigma} = \text{Constant} &\Rightarrow \langle \boldsymbol{\varepsilon} \rangle_{\Omega} = \langle \mathbb{E}^{-1} : \boldsymbol{\sigma} \rangle_{\Omega} = \langle \mathbb{E}^{-1} \rangle_{\Omega} : \langle \boldsymbol{\sigma} \rangle_{\Omega} \end{aligned} \tag{B8}$$

Consequently, we have

$\begin{aligned} (1) \quad \mathbf{u} _{\partial\Omega} = \mathcal{E} \cdot \mathbf{x}: \\ \text{Voigt: } \boldsymbol{\sigma} = \mathbb{E} : \mathcal{E}, \boldsymbol{\varepsilon} = \mathcal{E} \\ \text{Reuss: } \boldsymbol{\sigma} = \langle \mathbb{E}^{-1} \rangle_{\Omega} : \mathcal{E}, \boldsymbol{\varepsilon} = \mathbb{E}^{-1} : \langle \mathbb{E}^{-1} \rangle_{\Omega}^{-1} : \mathcal{E} \\ (2) \quad \mathbf{t} _{\partial\Omega} = \mathcal{L} \cdot \mathbf{n}: \\ \text{Voigt: } \boldsymbol{\varepsilon} = \langle \mathbb{E} \rangle^{-1} : \mathcal{L}, \boldsymbol{\sigma} = \mathbb{E} : \langle \mathbb{E}^{-1} \rangle_{\Omega} : \mathcal{L} \\ \text{Reuss: } \boldsymbol{\sigma} = \mathcal{L}, \boldsymbol{\varepsilon} = \mathbb{E}^{-1} : \mathcal{L} \end{aligned}$	$\tag{B9}$
--	------------

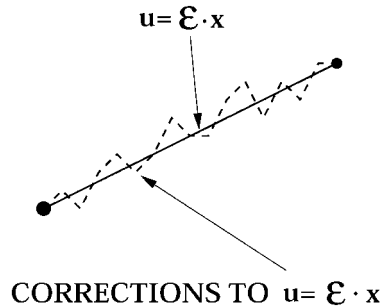


Figure C1. Krylov 'corrections' to a smooth 'Voigt' starting vector.

The following are points should be made clear about the Reuss assumption:

- highly oscillatory in the displacement field variable,
- kinematically inadmissible,
- statically admissible,

whereas the Voigt assumption is

- not oscillatory in the displacement field variable,
- kinematically admissible,
- statically inadmissible.

Therefore, from an iterative solver point of view, the Reuss field assumption is not of much value as a starting vector for a displacement-based variational method. Furthermore, such guess cannot be projected onto the initial nodal values because it is double valued at material discontinuities (not kinematically admissible). However, it is important to note that if a complementary-based numerical method were to be used, where the primary variable is the stress, the Reuss guess would be advantageous due to the smooth nature of stress field assumed. The Voigt constant strain assumption produces a low-frequency initial guess. Therefore, from an iterative solver point of view, it is of great value when using displacement-based variational principles such as the standard FEM. Furthermore, such a guess can easily be projected onto initial nodal values, because it is single valued. The central point is that each conjugate gradient iteration can be viewed as a microstructural 'corrector' to an initially statically inadmissible initial guess (Figure C1), and that $\mathbf{u}|_{\Omega} = \boldsymbol{\varepsilon} \cdot \mathbf{x}$ should be used for the displacement tests. Numerical results are presented in the body of the work (see Table III).

REFERENCES

1. Michaud V. Liquid state processing. In *Fundamentals of Metal Matrix Composites*, Suresh S, Mortensen A, Needleman A (eds). Butterworth-Heinemann 1992.
2. Mura T. *Micromechanics of Defects in Solids* (2nd edn). Kluwer Academic Publishers: Dordrecht, 1993.
3. Nemat-Nasser S, Hori M. *Micromechanics: Overall Properties of Heterogeneous Solids*. Elsevier: Amsterdam, 1993.
4. Jikov VV, Kozlov SM, Olenik OA. *Homogenization of Differential Operators and Integral Functionals*. Springer: Berlin, 1994.
5. Hill R. The elastic behaviour of a crystalline aggregate. *Proceedings of the Physical Society (London)* 1952; **A65**:349–354.

6. Zohdi TI, Feucht M, Gross D, Wriggers P. A description of macroscopic damage via microstructural relaxation. *International Journal for Numerical Methods in Engineering* 1998; **43**:493–507.
7. Reuss A. Berechnung der Fließgrenze von Mischkristallen auf Grund der Plastizitätsbedingung für Einkristalle. *Zeitschrift fuer angewandte Mathematik und Mechanik* 1929; **9**:49–58.
8. Voigt W. Über die Beziehung zwischen den beiden Elastizitätskonstanten isotroper Körper. *Wied. Ann.* 1889; **38**:573–587.
9. Hashin Z, Shtrikman S. On some variational principles in anisotropic and nonhomogeneous elasticity. *Journal of Mechanical Physics and Solids* 1962; **10**:335–342.
10. Hashin Z, Shtrikman S. A variational approach to the theory of the elastic behaviour of multiphase materials. *Journal of Mechanical Physics and Solids* 1963; **11**:127–140.
11. Huet, C. Application of variational concept to size effects in elastic heterogeneous bodies. *Journal of Mechanical Physics and Solids* 1990; **38**:813–841.
12. Zohdi TI, Wriggers P. A domain decomposition method for bodies with microstructure based upon material regularization. *International Journal of Solids and Structures* 1999; **36**(17):2507–2526.
13. Hughes TJR. *The Finite Element Method*. Prentice-Hall: Englewood Cliffs, NJ, 1989.
14. Axelsson O. *Iterative Solution Methods*. Cambridge University Press: Cambridge, 1994.
15. Briggs W. *A Multigrid Tutorial*, 1987, (Siam Issue).